Chemical Engineering Journal 423 (2021) 130186

Contents lists available at ScienceDirect

Chemical Engineering Journal

journal homepage: www.elsevier.com/locate/cej

# Substitution of Pb with $Mn^{2+}$/$Nd^{3+}$ to improve the luminescence and thermal stability of $Cs_4PbBr_6$

Wanying Zhang [a], Saroj Thapa [c], Yao Sun [a], Sydni Norville [c], Hongyang Zhu [b,*], Peifen Zhu [c,*], Guofeng Wang [a,*], Weiping Qin [d]

[a] Key Laboratory of Functional Inorganic Material Chemistry, Ministry of Education, School of Chemistry and Materials Science, Heilongjiang University, Harbin 150080, China
[b] School of Physics and Electronic Engineering, Linyi University, Linyi 276005, PR China
[c] Department of Physics and Engineering Physics, The University of Tulsa, Tulsa, OK 74104, USA
[d] College of Electronic Science and Engineering, Jilin University, Changchun 130012, China

ARTICLE INFO

*Keywords:*
Thermal stability
Luminescence enhancement
$Cs_4PbBr_6$
Metal ion doping
DFT calculation
white LEDs

ABSTRACT

Inorganic metal halide perovskites have superior properties compared to the existing hybrid organic metal halide perovskites, but the issue of poor stability has not been solved, which limits its practical applications. Here, our theoretical and experimental results show that $Cs_4PbBr_6$ has higher thermal stability than $CsPbBr_3$, especially, $Cs_4PbBr_6$ with higher stability was successfully achieved by $Mn^{2+}$ doping or $Mn^{2+}$/$Nd^{3+}$ co-doping. In addition to the high thermal stability mentioned above, $Mn^{2+}$ doped or $Mn^{2+}$/$Nd^{3+}$ co-doped $Cs_4PbBr_6$ has stronger luminescence intensity than pure $Cs_4PbBr_6$, which can be applied in white light-emitting diodes (LEDs). The doping of $Mn^{2+}$ can result in long-lifetime sensitized dopant luminescence and a magnetically coupled exciton state, which weakens the temperature quenching effect of luminescence. We have obtained white light emission by combining blue-emitting $CsPbBr_3$, green-emitting $Cs_4PbBr_6$:$Mn^{2+}$/$Nd^{3+}$ (or $Cs_4PbBr_6$:$Mn^{2+}$), yellow-emitting $CsPbBr_{0.5}I_{0.5}$, and red-emitting $Eu^{3+}$-doped metal–organic frameworks (MOF:$Eu^{3+}$). The white light shows an LER of 322 lm/W (or 336 lm/W) and a CRI above 90, which is excellent for indoor lighting applications.

## 1. Introduction

In the past few decades, artificial light sources have played a vital role in our daily life as they have been widely used in various lighting and display systems, anti-counterfeiting fields, and medicine [1–9]. Due to its higher luminous efficacy and longer life span compared to the traditional light sources, solid-state lighting is regarded as a next-generation light source that replaces traditional incandescent and fluorescent lamps [10–12]. Solid-state lighting devices are usually based on light-emitting diodes (LEDs) and are usually manufactured by coating inorganic phosphors on the surface of LED chips (so-called phosphor-converted LEDs) [13–19]. Therefore, developing high-efficiency phosphors with high stability is instrumental in further improving the performance of the manufactured white LED devices.

As the fourth-generation lighting equipment, the white LED has been widely concerned. It is well known that white light can be obtained by properly combining different color phosphors, therefore, the research community has been committed to the development of three primary color phosphors for white LEDs [20–25]. Among the reported phosphors, inorganic halide perovskite nanocrystals have attracted great attention due to their excellent properties in tunable, narrow linewidth emission, and high photoluminescence quantum yield (PLQY) [26]. As a member of inorganic halide perovskite nanomaterials, cubic phase $CsPbBr_3$ has been widely studied because of its better performance than its organic counterpart, but its poor stability due to the low formation energy of the perovskite lattice has not been solved, which limits its further applications [27–29]. Although various methods were used to improve the stability of $CsPbBr_3$, its thermal stability still seriously affects its practical applications. Compared with cubic phase $CsPbBr_3$, $Cs_4PbBr_6$ has a rhombohedral phase ($R\bar{3}c$ (ICSD 73–2478) space group) structure, which can show strong green photoluminescence (PL). The obtained luminescence from $Cs_4PbBr_6$ may be due to the halogen-related

* Corresponding authors at: Key Laboratory of Functional Inorganic Material Chemistry, Ministry of Education, School of Chemistry and Materials Science, Heilongjiang University, Harbin 150080, China (G. Wang); School of Physics and Electronic Engineering, Linyi University, Linyi 276005, China (H. Zhu); Department of Physics and Engineering Physics, The University of Tulsa, Tulsa, OK 74104, USA (P. Zhu).
*E-mail addresses:* zhuhongyang@lyu.edu.cn (H. Zhu), peifen-zhu@utulsa.edu (P. Zhu), 2010070@hlju.edu.cn (G. Wang).

https://doi.org/10.1016/j.cej.2021.130186
Received 15 February 2021; Received in revised form 7 April 2021; Accepted 30 April 2021
Available online 5 May 2021

defect states within the bandgap, which act as radiative recombination centers for the excitons trap. However, there are few reports on the stability and fluorescence of $Cs_4PbBr_6$. Besides, it is well known that Pb is a harmful element, it is outmost to remove it. In the reported work, most of the people focused on replacing the Pb in $CsPbBr_3$. In this work, we reported the replacement of the Pb with Mn/Nd in $Cs_4PbBr_6$ and investigated their photophysical properties and stability.

It is well known that the luminescent intensity of phosphor is an important factor affecting the application of phosphor in white LEDs. Rare-earth ions are widely used in many fields because of their special electronic structure and unique physical and chemical properties [30–42]. It is expected to obtain phosphors with high stability and high fluorescence intensity by introducing rare-earth ions into inorganic halide perovskite nanomaterials.

Therefore, we took lead cesium bromide with different phases ($CsPbBr_3$ and $Cs_4PbBr_6$) as the research focus and introduce different ions of appropriate elements into the crystal lattice to achieve the purpose of obtaining high-stability and high-quality phosphors. Firstly, the properties of the materials were studied by the theoretical simulation method, and then the research scheme was designed according to the theoretical results. As expected, $Cs_4PbBr_6$ was successfully synthesized, which is more stable than $CsPbBr_3$. Further, $Cs_4PbBr_6$ with higher stability as well as stronger luminescence intensity was successfully achieved by $Mn^{2+}$ doping or $Mn^{2+}/Nd^{3+}$ co-doping. The novel white LED device structure was designed by the combination of stable red-emitting MOF: $Eu^{3+}$, yellow-emitting $CsPbBr_{0.5}I_{0.5}$, green-emitting $Cs_4PbBr_6$: $Mn^{2+}/Nd^{3+}$, and blue-emitting $CsPbBr_3$. The spectral optimization was then carried out to obtain white light with excellent vision performance and superior color quality. Subsequently, we fabricated the white LEDs and tested device performance. Our findings show that $Mn^{2+}/Nd^{3+}$ co-doped CsPbBr6 is an excellent green-emitting phosphor that can be used in III-nitride-based white LEDs to achieve stable white light emission.

## 2. Results and discussion

To study the stability of $CsPbBr_3$, $Cs_4PbBr_6$, and $Cs_4MnBr_6$, the crystal structures of these materials were optimized first by using first-principles density functional theory (DFT), as shown in Figure S1 in the electronic supporting information (ESI). The stability of compounds was evaluated by the change in the Gibbs free energy between reactants and products [43] by using the following equations:

$$Cs_4PbBr_6 \rightleftharpoons 4CsBr + PbBr_2 \tag{1}$$

$$CsPbBr_3 \rightleftharpoons CsBr + PbBr_2 \tag{2}$$

The enthalpy change at zero temperature was calculated based on the DFT total energy.

$$\Delta H^{o}_{0K} \approx \sum_{i}^{products} n_i E_{tot}[i] - \sum_{j}^{reac} n_j E_{tot}[j] \tag{3}$$

$$\begin{aligned}\Delta H^{O}_{0K_{Cs_4PbBr_6}} &\approx [4 \\ &\times (-6.025080)eV + (-9.572600)eV] - (-34.457497)eV \\ &= 0.7846eV\end{aligned} \tag{4}$$

$$\begin{aligned}\Delta H^{O}_{0K_{CsPbBr_3}} &\approx [(-6.025080)eV + (-9.572600)eV] - (-15.884947)eV \\ &= 0.2873eV\end{aligned} \tag{5}$$

The decomposition reaction enthalpy was calculated from equation (2). High values favor the stability of perovskites. A higher value means that the compound needs to absorb more energy to be decomposed. A negative value means the final products have lower energy and means that this compound does not need to absorb energy to be decomposed. Our computational results showed that $Cs_4PbBr_6$ is more stable than $CsPbBr_3$. The calculated Vienna Ab-initio Simulation Package (VASP) energy (Table S1 and Figure S1 in the ESI) were −34.45749, −36.33309, and −38.48185 eV for $Cs_4PbBr_6$, $Cs_4MnBr_6$, and $Cs_4Nd_{0.5}Mn_{0.5}Br_6$, indicating that $Cs_4MnBr_6$ or $Cs_4Nd_{0.5}Mn_{0.5}Br_6$ is more stable than $Cs_4MnBr_6$. Thus, the stability of $Cs_4PbBr_6$ can be improved by $Mn^{2+}/Nd^{3+}$ co-doping. To evaluate the dynamic stability, the phonon properties are calculated. The phonon dispersion curves (Figure S2) show that the virtual frequency appears in the frequency spectra of $CsPbBr_3$ and $Cs_4PbBr_6$, but not in the frequency spectrum of $Cs_4MnBr_6$. Therefore, the $Cs_4MnBr_6$ sample is the most stable one.

Fig. 1i shows the charge density difference for $CsPbBr_3$, $Cs_8Pb_2Br_{12}$, $Cs_8PbMnBr_{12}$, $Cs_8Mn_2Br_{12}$, and $Cs_8NdMnBr_{12}$. That is the difference in charge density between the self-consistent pseudo charge density and the superposition of atomic charge densities. The color bar represents the charge density. A negative charge density means electrons were lost and a positive charge density means electrons were gained. In general, Br gains electrons. Pb, Mn, and Nd lose electrons. Pb is much more easily losing electrons than Mn. Nd is the most easily losing electrons than Mn or Pb. The electron localization function (ELF) provides a new description of the chemical bond for almost all classes of compounds. ELF is a three-dimensional real space function with a numerical range of 0 to 1. In the area surrounded by the equivalent of ELF with higher value, the electron has strong localization and is not easy to run out. In the area surrounded by the equivalent of ELF with lower value, the electron localization is weak and the electron is easy to delocalize to other regions. The value of ELF = 0.5 corresponds to the electron–gas-like pair probability [44]. Here, the ELF was used to analyze the chemical bonding, as shown in Fig. 1ii. The surface is cut on the boundary of the primitive cell. Fig. 1iii shows the cross-sectional plot of ELF for $CsPbBr_3$, $Cs_8Pb_2Br_{12}$, $Cs_8PbMnBr_{12}$, $Cs_8Mn_2Br_{12}$, and $Cs_8NdMnBr_{12}$. The results indicated that the Br and Cs are localized in the area surrounded by the equivalent of ELF with higher value, indicating that the charges localized around Br and Cs. While, the Pb, Mn, and Nd are localized in the area surrounded by the equivalent of ELF with lower value, and thus, the ionic bonding formed between Pb/Mn/Nd and Br. The charge analysis showed that the net charge on Pb and Br is 0.88 and −0.70, respectively in $Cs_4PbBr_6$, while the net charge on Mn and Br is 0.83 and −0.68, respectively in $Cs_4MnBr_6$. Besides, the net charge on Nd and Mn is 1.26 and 0.79, respectively in $Cs_8NdMnBr_{12}$.

By replacing $Pb^{2+}$ with $Mn^{2+}$ in $Cs_4Pb_2Br_{12}$, the bandgap decreased from 3.90 eV to 2.66 eV, which is attributed to the $Mn^{2+}$ (Fig. 2). The corresponding density of states of $Cs_8Pb_2Br_{12}$, $Cs_8PbMnBr_{12}$, $Cs_8Mn_2Br_{12}$, and $Cs_8NdMnBr_{12}$ are also shown in Fig. 2, which is consistent with bandstructure. For comparison, the theoretical simulation of band structure and density of states for $CsPbBr_3$ were shown in Figure S3 in the ESI. Thus, the bandgap energy of $Cs_8Pb_xMn_{2-x}Br_{12}$ could be engineered by tuning the ratio of Mn to Pb, which is consistent with our experimental results. Besides, the bandgap of $Cs_8NdMnBr_{12}$ was only 1.01 eV, indicating that the bandgap energy of $Cs_8Nd_xMn_{2-x}Br_{12}$ could be further engineered by tuning the ratio of Mn to Nd.

The theoretical simulation results of the optical properties for $Cs_8Nd_2Br_{12}$, $Cs_8NdMnBr_{12}$, $Cs_8Mn_2Br_{12}$, $Cs_8PbMnBr_{12}$, and $Cs_8Pb_2Br_{12}$ are shown in Fig. 3. The frequency-dependent complex dielectric function was calculated using the first-principles density functional theory implemented in the VASP package. The results indicated that the optical properties of $Cs_8Nd_2Br_{12}$, $Cs_8Pb_2Br_{12}$, and $Cs_8Mn_2Br_{12}$ are completely different, and the $Cs_8PbMnBr_{12}$ takes into account the properties of both $Cs_8Pb_2Br_{12}$ and $Cs_8Mn_2Br_{12}$ materials. Similarly, $Cs_8NdMnBr_{12}$ should take into account the properties of both $Cs_8Nd_2Br_{12}$ and $Cs_8Mn_2Br_{12}$ materials. These spectral results show that we can engineer material properties by tuning the ratio of Mn (Nd) to Pb to be applied in novel optoelectronic devices including white LEDs and improve the performance of devices.

The energy of $Cs_4PbBr_6$ with different crystal planes is shown in Table S2 in the ESI. The results show that the 101 plane has the lowest energy, which is more stable. This is consistent with our high-resolution TEM images, which will be discussed later in detail. The work function

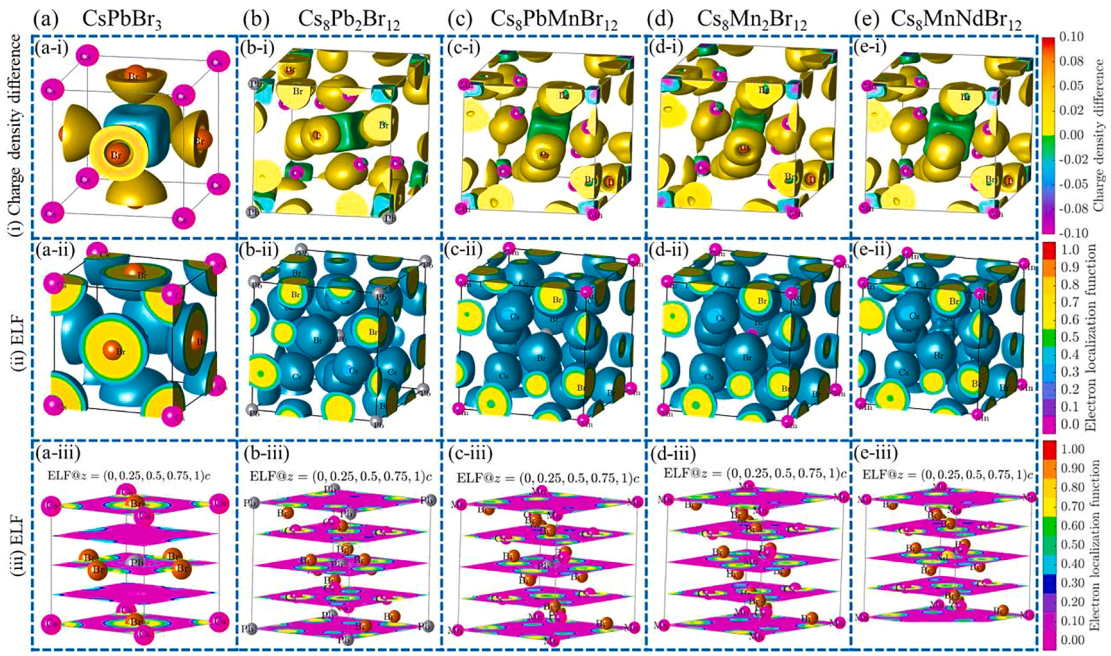


**Fig. 1.** (i) Deformation charge density, (ii) electron localization function (ELF), and (iii) cross sectional plots of ELF for $CsPbBr_3$, $Cs_8Pb_2Br_{12}$, $Cs_8PbMnBr_{12}$, $Cs_8Mn_2Br_{12}$, and $Cs_8MnNdBr_{12}$.

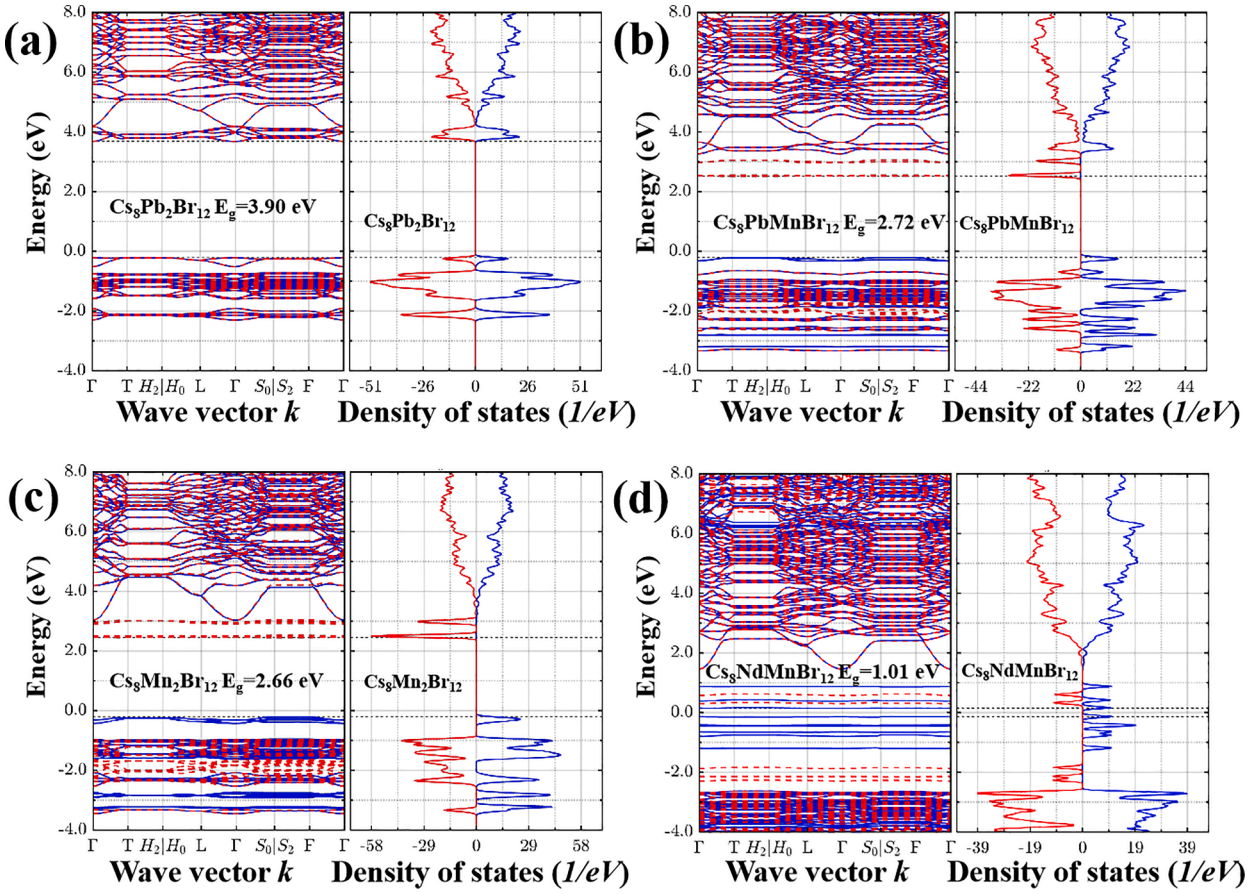


**Fig. 2.** Theoretical simulation of band structure and density of states for (a) $Cs_8Pb_2Br_{12}$, (b) $Cs_8PbMnBr_{12}$, (c) $Cs_8Mn_2Br_{12}$, and (d) $Cs_8NdMnBr_{12}$.

of 101 planes is 4.367 eV. By replacing one of Pb with Mn in $(Cs_4PbBr_6)_{16}$ with 101 planes, the energy decreases to –33.5722 eV, and the work function increases to 4.434 eV.

The size and morphology of the materials were characterized by the transmission electron microscope (TEM, Fig. 4a) and scanning electron microscope (SEM, Figure S5 in the ESI) images. After Mn doping, there

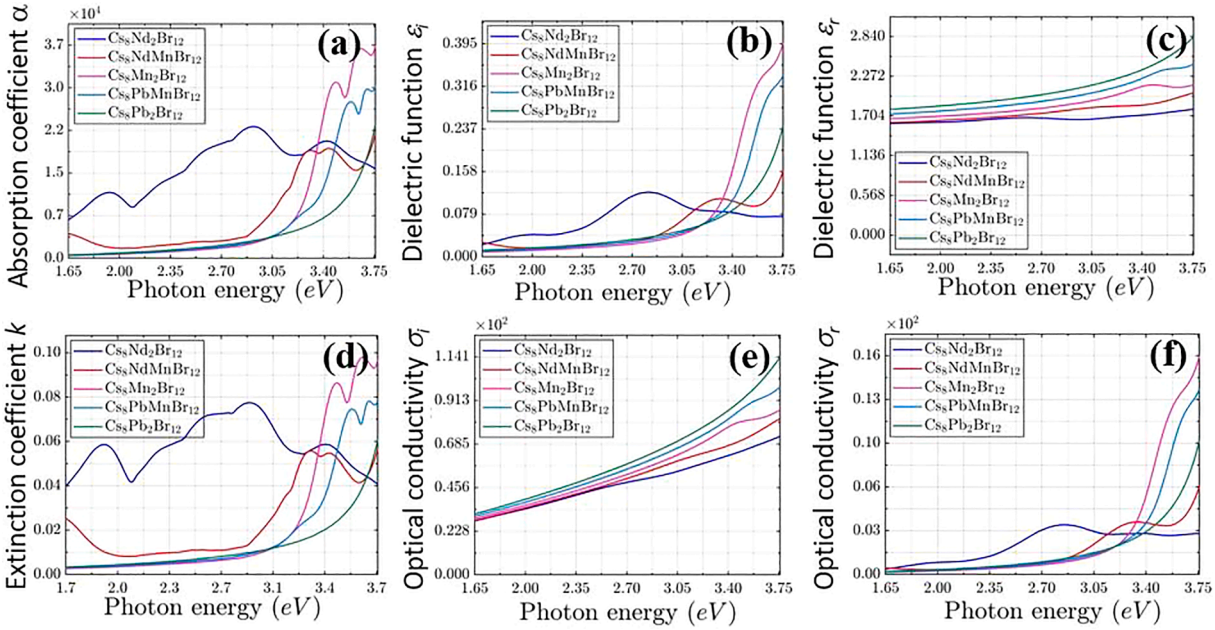


**Fig. 3.** Theoretical simulation of optical properties for $Cs_8Nd_2Br_{12}$, $Cs_8NdMnBr_{12}$, $Cs_8Mn_2Br_{12}$, $Cs_8PbMnBr_{12}$, and $Cs_8Pb_2Br_{12}$: (a) absorption coefficient, (b, c) dielectric function, (d) extinction coefficient, and (e, f) optical conductivity.

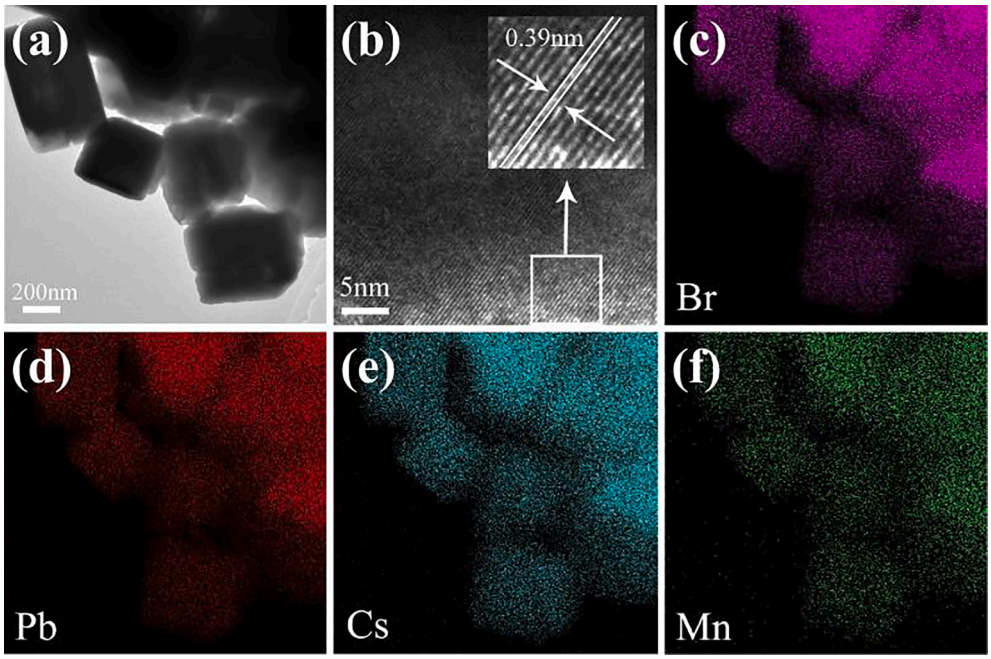


**Fig. 4.** (a, b) TEM and HRTEM images of CPB-3Mn. (c-f) The corresponding elemental mappings of Br, Pb, Cs, and Mn in CPB-3Mn.

was no obvious change in the morphology of $Cs_4PbBr_6$ (CPB) particles. The HRTEM images show that the lattice distance of $Cs_4PbBr_6$:3%$Mn^{2+}$ (CPB-3Mn) is 3.90 Å, which is attributed to the (1 0 1) crystalline plane of CPB. The results of the element mapping (Fig. 3) of CPB-3Mn indicate that Br, Pb, Cs, and Mn are uniformly distributed in CPB-3Mn. Importantly, it can be seen that Mn is evenly distributed throughout the CPB.

The results of the XRD patterns (Fig. 5a) of samples with different $PbBr_2$:CsBr molar ratios show that pure rhombohedral phase $Cs_4PbBr_6$ (JCPDS 73–2478) was obtained only when the $PbBr_2$:CsBr molar ratio was 1:4, and the phase of $Mn^{2+}$ doped $Cs_4PbBr_6$ remained unchanged after calcined at 200 °C. Thus, $Mn^{2+}$ doped $Cs_4PbBr_6$ has high thermal stability. Besides, because the ionic radius of Mn is much smaller than that of Pb, Mn can easily replace Pb [28]. This indicates that $Mn^{2+}$ is introduced into the crystal lattice of CPB, where $Mn^{2+}$ occupy the $Pb^{2+}$ positions. The phase of $Mn^{2+}/Ln^{3+}$ co-doped $Cs_4PbBr_6$ also remains unchanged (Fig. 5b). The thermal stability was further measured by using the thermal analyzer (TGA) and differential scanning calorimetry (DSC) method (Fig. 5c and Figure S6a in the ESI), illustrating the enhanced thermal stability of perovskite materials due to the doping and co-doping of $Mn^{2+}$ and $Mn^{2+}/Ln^{3+}$ ions under a nitrogen atmosphere. Specifically, it can be seen from Figure S6a in the ESI that the CPB material begins to exothermic at 493 °C, indicating that the material begins to decompose and loses its weight completely at 730 °C. After $Mn^{2+}$ doping (CPB-3Mn), the decomposition temperature increased

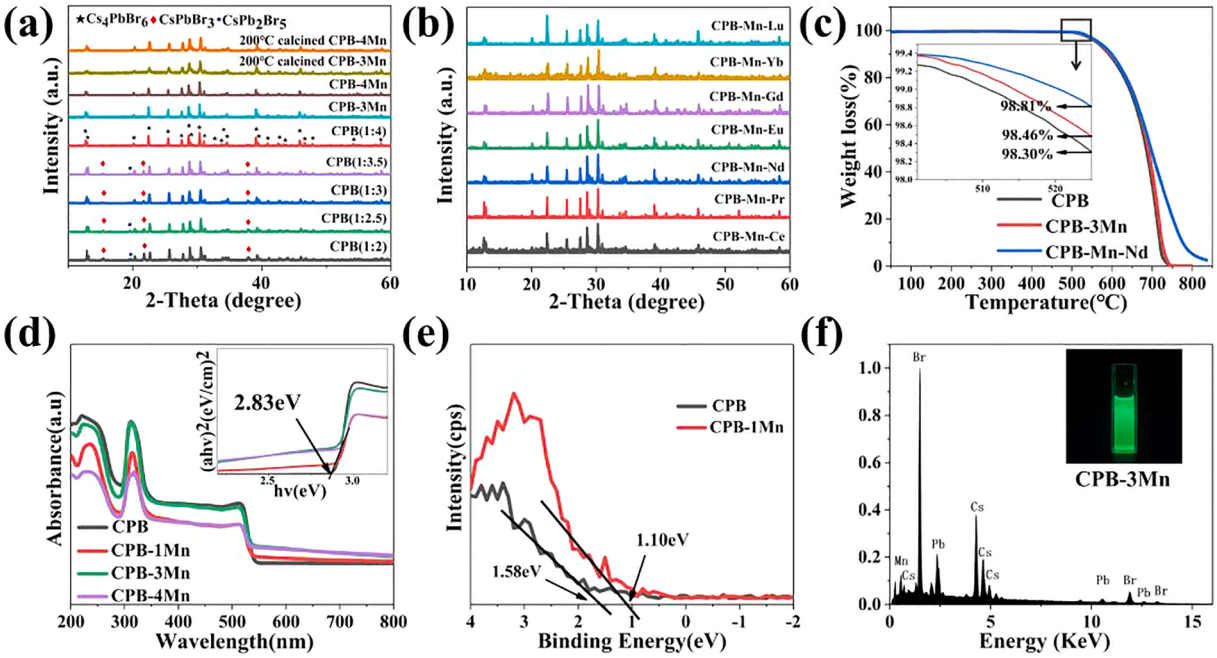


**Fig. 5.** (a) XRD patterns of samples with different $PbBr_2$:CsBr ratios and different $Mn^{2+}$ doping concentrations. (b) XRD patterns of $Ln^{3+}/Mn^{2+}$ co-doped $Cs_4PbBr_6$. (c-f) TGA curves, UV–vis diffuse reflectance spectra, and band gaps patterns (inset), valence band XPS spectra, and EDS quantitative analysis.

slightly to 496 °C, and the weight was completely lost at 747 °C. After being co-doped with $Mn^{2+}$ and $Nd^{3+}$, the material has not completely lost weight at 833 ℃, confirming the decrease decomposition rate and increase thermal stability (Fig. 5c). Note that the thermal stability of Cs4PbBr6 is comparable to the reported work, [1-3] however, the thermal stability of Mn and Mn/Nd co-doped samples shows much higher thermal stability.

The bandgap energy is directly related to the absorption of light by the semiconductor. The smaller the energy gap, the larger the light absorption range. The absorption spectra were used to study the effect of the doped $Mn^{2+}$ concentration on the bandgap of samples, as depicted in Fig. 5d. The effective absorption of these nanocrystals is in the UV–visible range, and the bandgap of the material can be engineered by changing the concentration of doped $Mn^{2+}$, which is consistent with our calculation results. The peaks in the absorption spectra are due to exciton absorption.

Fourier transform infrared (FT-IR) spectroscopy was also performed to extract the structural information of the CPB and CPB-3Mn (Figure S6b in the ESI). The characteristic peaks at 540 $cm^{-1}$ are attributed to the stretching vibration of C-Br. The characteristic peaks at 1049 and 1435 $cm^{-1}$ are attributed to the stretching vibration of alcohol Vc-o and the in-plane bend of H-O, respectively. The characteristic peaks at 2932 and 3446 $cm^{-1}$ are attributed to the C–H stretching vibration of $–CH_2-$ and the stretching vibration of N–H, respectively. Fig. 5e presents the corresponding XPS valence band spectra of CPB and CPB-1Mn. The valence band positions of the CPB and CPB-3Mn were calculated to be ~ 1.58 and ~ 1.1 eV, respectively. The EDS quantitative analysis of samples is shown in Fig. 5f and Figure S7 in the ESI. It can be seen from EDS that with the doping of $Mn^{2+}$, the peak area of the Mn element gradually increases, which further shows that $Mn^{2+}$ is successfully doped into CPB. We also carried out the EDS measurements on $Mn^{2+}$ and $Nd^{3+}$ co-doped samples, and the results show that both ions were successfully doped into the material. For the experimental results, the results of the ICP-MS test indicate that the doping amount of $Mn^{2+}$ was 4.5 mol%, and the doping amount of $Nd^{3+}$ was 0.43 mol%. For the theoretical calculation results, we can build a supercell to reduce the doping concentration. However, if the size of the supercell is too large, the calculation time will be very long. Due to the limitations of my calculation capability, we could not perform large supercell calculations. Note that the calculation only provides the guidelines for performing the experiments. The trend obtained from the calculation is consistent with our experimental results.

To verify the presence of Mn in $Cs_4PbBr_6$:$Mn^{2+}$, we perform X-ray photoelectron spectroscopy (XPS) measurements on films of CPB-3Mn. The full XPS spectra (Figure S8 in the ESI) showed that the surface of CPB-3Mn is covered with Br, Pb, Cs, Mn, and a small amount of C element. Based on XPS analysis, the element content of Cs, Pb, Br, and Mn for CPB-3Mn is calculated to be 11.41 at%, 4.55 at%, 29.63 at%, and 3.88 at%, respectively, which agrees with the EDS results (Fig. 5f). The high-resolution XPS spectra of CPB-3Mn are shown in Figure S9 in the ESI. The spectra of Br 3d (Figure S9a in the ESI) show the two peaks located at 68 and 69.5 eV which can be attributed to characteristic peaks corresponding to Br $3d_{5/2}$ and Br $3d_{3/2}$, respectively. Similarly, the high-resolution spectrum of Pb 4f (Figure S9b in the ESI) consists of two characteristic peaks of Pb $4f_{7/2}$ at 138.2 eV and Pb $4f_{5/2}$ at 143 eV. Besides, Figure S9c in the ESI represents the characteristic peak of Cs $3d_{5/2}$ at 726 eV and Cs $3d_{3/2}$ at 740.6 eV. Finally, the characteristic peaks of Mn 2p (Figure S9d in the ESI) corresponding to Mn $2P_{3/2}$ at 643.9 eV and Mn $2P_{1/2}$ at 652.3 eV conclude that $Mn^{2+}$ ions successfully enter the lattice site of the $Cs_4PbBr_6$ perovskites.

All of the emission spectra shown in Fig. 6 are collected at a fixed excitation wavelength of 361 nm. Fig. 6a shows the emission spectra of CPB with different $PbBr_2$:CsBr ratios, indicating that the pure $Cs_4PbBr_6$ ($PbBr_2$:CsBr = 1:4) has the best luminescence performance. With increased $Mn^{2+}$ concentrations the excitonic luminescence of CPB-Mn was detected to increase first and then decrease, which is shown in Fig. 6b. Mn doping can generate long-lifetime sensitized dopant luminescence and create a magnetically coupled exciton state, as shown in Fig. 6c. These properties mainly result from the strong exchange interaction between the charge carriers of the host material and the d electrons of the Mn dopant, which allows excitation energy transfer or creates new coupled electronic states between the exciton and dopant. In lead halide perovskite, the high tolerance for trap states creates much more chance for promoting the excitation energy transfer to Mn *d*-states and, consequently, Mn $d - d$ emission. Under ultraviolet excitation, Mn-doped CPB shows bright green luminescence due to the Mn *d*-

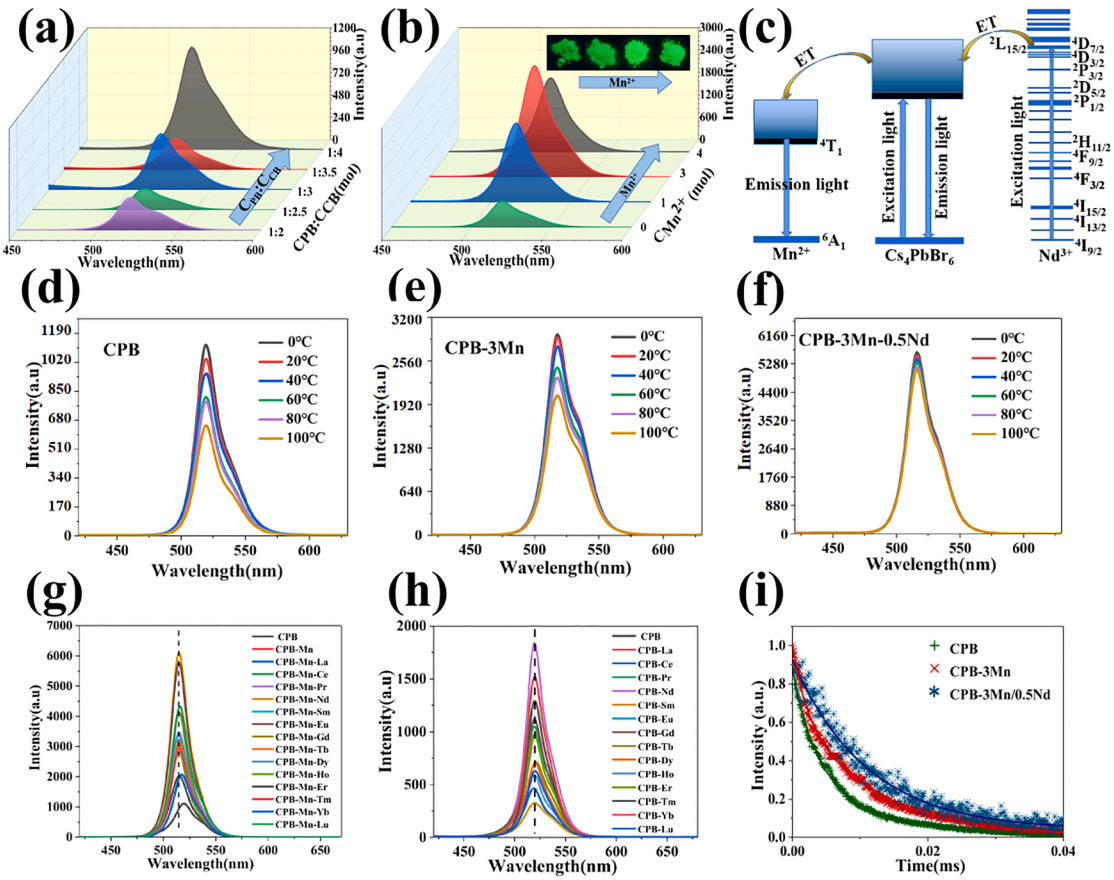


**Fig. 6.** (a, b) Emission spectra of CPB with different $PbBr_2$:CsBr and different $Mn^{2+}$ doping concentrations mole ratios under 361 nm excitation. (c) Luminescence mechanism of $Ln^{3+}/Mn^{2+}$ co-doped $Cs_4PbBr_6$. (d-f) Temperature-dependent emissions spectra of CPB, CPB-3Mn, and $Nd^{3+}/Mn^{2+}$ co-doped CPB. (g) Emission spectra of $Ln^{3+}/Mn^{2+}$ co-doped CPB. (h) Emission spectra of $Ln^{3+}$ doped CPB. (i) Luminescence decay curve for the CPB, CPB-3Mn, and CPB-3Mn/0.5Nd samples.

*d* transition. Note that the temperature-dependent spectra were normalized. The shoulders of $Cs_4PbBr_6$:$Mn^{2+}$ are the most obvious because the emissions of $Mn^{2+}$ and $Cs_4PbBr_6$ are partially overlapped. Besides, the full width at half maximum (FWHM) of all the samples does not change significantly. Thus, the color purity has not been significantly reduced, further verifying that the stability of the material has been improved. The excitation spectra monitored at 520 nm that of CPB prepared with different $PbBr_2$:CsBr molar ratios and different $Mn^{2+}$ concentrations are shown in Figure S10 in the ESI. These spectra are almost identical in shape and encompass the emission range (325–525 nm) of UV/blue LED chips. The result indicates that the as-synthesized perovskite materials can be used as the color conversion layer to design the wLED when combined with UV/blue LED chips.

Temperature is generally considered to be one of the main parameters that regulate ion fluorescence emission. The temperature-dependent spectra of CPB, $Mn^{2+}$ doped CPB, and $Mn^{2+}/Nd^{3+}$ co-doped CPB under 361 nm excitation were studied, as shown in Fig. 6d-f. The fluorescence quenching caused by this temperature comes from the enhancement of the non-radiative relaxation of the previous energy level and the population of adjacent metastable states. Compared with CPB and $Mn^{2+}$ doped CPB, the $Mn^{2+}/Nd^{3+}$ co-doped CPB has the best fluorescence thermal stability. Moreover, no obvious change in luminescence intensity was observed from $Mn^{2+}/Nd^{3+}$ co-doped CPB compared to that of CPB. We also tested the spectra of other rare-earth ions doped and co-doped materials (Fig. 6g and h). The results indicated that the $Mn^{2+}/Nd^{3+}$ co-doped CPB has the strongest luminescence. The luminescence enhancement of $Nd^{3+}$ doped samples can be attributed to the fact that rare-earth ions can regulate the local microstructure and local symmetry of the materials. Besides, there is energy transfer between $Mn^{2+}$ and rare-earth ions, so the optical properties of the materials can be further optimized (Fig. 6c). The excitation spectra of $Ln^{3+}$ doped and $Ln^{3+}/Mn^{2+}$ co-doped CPB monitored at 520 nm are shown in Figure S11 in the ESI. These spectra are almost identical in shape and encompass the emission range (325–525 nm) of UV/blue LED chips, indicating the materials' favorability for color conversion layer in designing the WLEDs with a wide range of excitation. Fig. 6i presents the luminescence decay curves for the CPB, CPB-3Mn and $Cs_4PbBr_6$:3%$Mn^{2+}$/0.5%$Nd^{3+}$ (CPB-3Mn/0.5Nd), which can assess the photogenerated carrier lifetime. The lifetime of CPB-3Mn/0.5Nd is larger than those of CPB and CPB-3Mn. The photoluminescence quantum yields of $Cs_4PbBr_6$, $Cs_4PbBr_6$:$Mn^{2+}$, and $Cs_4PbBr_6$:$Mn^{2+}/Nd^{3+}$ are 49%, 59%, and 68%, respectively.

To study the potential application of these materials in solid-state lighting, herein, we proposed a device structure for white light emission, which is schematically shown in Fig. 7a. In brief, the device structure consists of the color conversion layer designed using the different color emitting perovskites materials (blue, green, and yellow) and MOF: $Eu^{3+}$ (red-emitting) that were optically pumped with a UV LED chip. The green-emitting $Cs_4PbBr_6$:$Mn^{2+}$ was sandwiched between the blue-emitting $CsPbBr_3$ and the yellow-emitting $CsPb(Br_{0.5}I_{0.5})_3$ to prevent anion exchange. The blue and yellow emitting perovskite materials were synthesized using the synthesis approach reported by our group and provided in detail in the experimental procedures in the ESI [20]. The MOF: $Eu^{3+}$ was deposited on top of $CsPb(Br_{0.5}I_{0.5})_3$ to improve the atmosphere stability of $CsPb(Br_{0.5}I_{0.5})_3$. The perovskite nanocrystals and MOF:Eu absorb UV light from near-UV LED chip to emit white light. Then, we systematically performed the spectral optimization of the designed device structure following our previous calculations [45,46]. The optical properties obtained from the extensive calculations and optimizations are summarized in Table S4 in the ESI and presented in

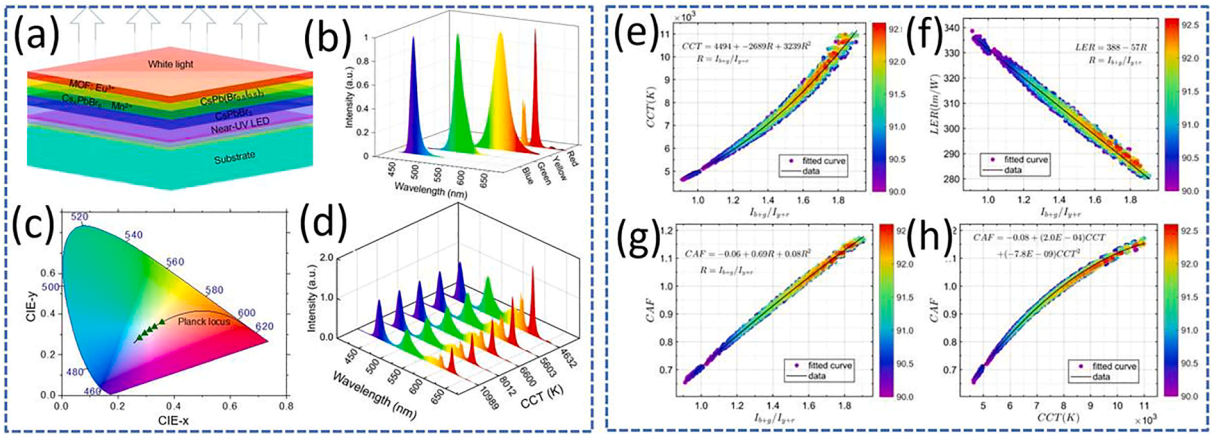


**Fig. 7.** (a) The schematic white LED device structure. (b) Emission spectra of red-emitting MOF: $Eu^{3+}$, yellow-emitting perovskites, green-emitting $Cs_8Pb_xMn_{2-x}Br_{12}$, and blue-emitting $CsPbBr_3$. (c) The chromaticity coordinates of white light in the CIE 1931 chromaticity diagram. (d) The spectral power distribution of white light with various CCTs (2989–9903 K). (e-g) CCT, LER, and CAF as a function of ratios of the sum of blue and green ($Cs_8Pb_xMn_{2-x}Br_{12}$) emissions to the sum of yellow and red emissions, respectively. (h) CAF changes with various CCTs (4632–10989 K). The color bar indicates the CRI.

Fig. 7b-d.

The calculations show that the LED structure with this configuration results in white light with an extremely high color rendering index (CRI > 90), high luminous efficacy (LER up to 336 lm/W), and correlated color temperature (CCT) tuned from 4632 to 10989 K (Table S4 in the ESI). Table S4 in general summarizes the different optical properties of five different optimized LEDs. The earlier studies have reported that a light source with CRI > 90 is highly suitable for indoor lighting applications [41]. The International Commission on Illumination (CIE) coordinates of these LEDs provided with the extremely small $D_{uv}$ and spectral power distributions indicate no obvious deviation from the Planckian locus (Fig. 7c). This suggests that as-obtained white light is comfortable for human eyesight even when exposed for a long time. A CCT of 4632 K of white light was obtained at power ratios of 1:1.37:1.06:1.52, and the corresponding LER is 336 lm/W. White light with the CIE coordinates of (0.330, 0.337) and the CCT of 5603 K was obtained by decreasing green, yellow, and red emission. The tunable CCT of white light could be obtained by tuning ratios of different emissions as shown in Fig. 7 (d). Increasing the ratio of red emission results in low CCT, which is warmer white light emission. Additionally, the CCT, LER, and circadian action factor (CAF), were affected by tuning the amount ratio of the blue and green-emitting materials to that of yellow and red-emitting materials, as shown in Fig. 8. At a larger ratio, higher CCT (Fig. 8a), lower LER (Fig. 8b), and higher CAF (Fig. 8c) could be obtained. The CAF can also be increased or decreased by increasing or decreasing the CCT, respectively (Fig. 8d).

Next, we also studied the application of $Cs_4PbBr_6$:$Mn^{2+}$/$Nd^{3+}$ in white LEDs (Fig. 8, Table S5 in the ESI). Here, we replaced $Cs_4PbBr_6$:$Mn^{2+}$ with $Cs_4PbBr_6$:$Mn^{2+}$/$Nd^{3+}$ without altering any optimization conditions in the devices mentioned above. The optical properties obtained from the extensive calculations and optimizations for five different LEDs are summarized in Table S5 in the ESI and presented in Fig. 8b-d. The estimates show that the LED structure with this configuration results in white light with high CRI (>90), LER (up to 322 lm/W), and CCT tuned from 5908 to 10360 K (Table S5 in the ESI). The CIE coordinates of the LEDs provided with the extremely small $D_{uv}$ indicate no apparent deviation from the Planckian locus (Fig. 7c). This suggests that as-obtained white light is comfortable for human eyesight even when exposed for a long time. White light with CCT of 5908 K and LER of 322 lm/W is obtained at power ratios of 1:0.81:0.38:1.03. The tunable CCT of white light could be obtained by tuning ratios of different emissions as shown in Fig. 7 (d). We notice that increasing the ratio of red emission results in low CCT, warmer white light, and vice-versa. The CCT, LER, and circadian action factor (CAF), were affected by tuning the amount ratio of the blue and green-emitting materials to that of yellow and red-emitting materials shown in Fig. 8.

We used different materials to build different white LED devices, which shows that the synthesized materials have good application in white LEDs. Note that there is still a lot of room for improvement in the assembly process of white LED, and we will make further optimization in

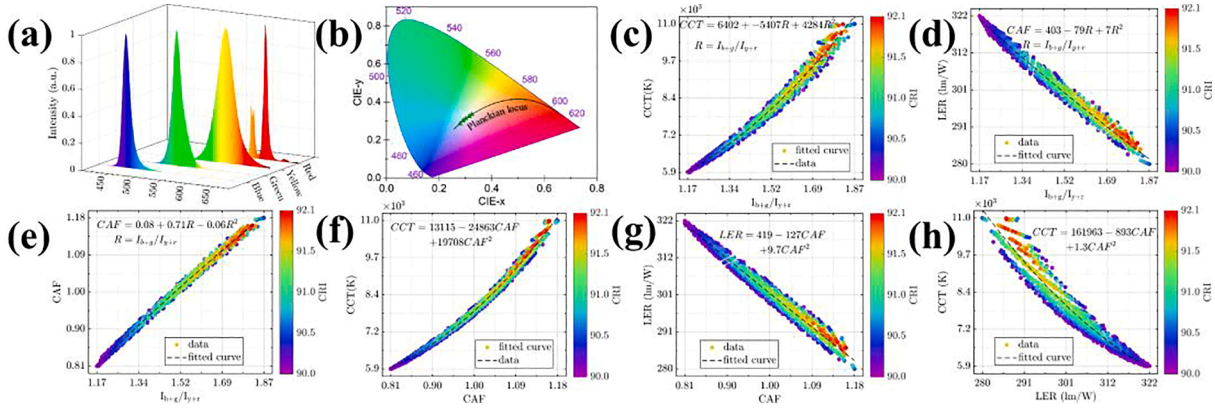


**Fig. 8.** (a-c) CCT, LER, and CAF as a function of ratios of the sum of blue and green ($Cs_4PbBr_6$:$Mn^{2+}$/$Nd^{3+}$) emissions to the sum of yellow and red emissions, respectively. (d, e) CCTs (4632–10989 K) and LER changes with various CAF. (f) CCTs (5908–10360 K) changes with various LER. The color bar indicates the CRI with the corresponding CCT.

future work. The detailed performance of white LEDs constructed by different samples has been summarized in Table S6. To further prove the stability of white LED, the time-dependent luminescence intensity (integral area) of wLED devices was studied (Figure S13). The decay rate of light intensity for the white LED constructed by $Cs_4PbBr_6$ is the fastest. The decay rate of light intensity for white LED constructed by $Mn^{2+}$/$Nd^{3+}$ co-doped $Cs_4PbBr_6$ is the slowest, which further proves the stability of white LED constructed by $Mn^{2+}$/$Nd^{3+}$ co-doped $Cs_4PbBr_6$ is the best. It is noted that the green emission increases with time, which is attributed to the redshift of the blue emission. Here, we only focus on the green luminescence samples in this work, and the blue light weakening and redshift are not the focus of this work. We will improve the stability of blue-emitting perovskite in our future work. The PL intensities of different samples under air, water, and UV radiation conditions were measured to indicate stability. The results indicated that the luminous intensity of $Mn^{2+}$/$Nb^{3+}$ doped $Cs_4PbBr_6$ was the most stable one (Figure S14).

## 3. Conclusion

In conclusion, we take lead cesium bromide with different phases ($CsPbBr_3$ and $Cs_4PbBr_6$) as the research focus and introduce different ions into the crystal lattice to achieve the purpose of obtaining high-stability and high-quality phosphors. Both theoretical and experimental results show that $Cs_4PbBr_6$ has good stability and strong luminescence performance. After being doped with $Mn^{2+}$, the stability and luminescence intensity of the material have been further improved. Especially, $Cs_4PbBr_6$ with higher stability as well as stronger luminescence successfully achieved by $Mn^{2+}$/$Nd^{3+}$ co-doping. Compared with $CsPbBr_3$, the strong exchange interaction between the charge carriers of the host material and d electrons of the Mn dopant allows either excitation energy transfer or creates new coupled electronic states between the exciton and dopant. Mn doping can generate long-lifetime sensitized dopant luminescence and create a magnetically coupled exciton state, which weakens the temperature quenching effect of luminescence. By using $Cs_4PbBr_6$:$Mn^{2+}$ or $Cs_4PbBr_6$:$Mn^{2+}$/$Nd^{3+}$ as the green-emitting material, MOF-$Eu^{3+}$ as the red-emitting material, and $CsPb(Br_{0.5}I_{0.5})_3$ as the yellow-emitting material in the white LED, we have achieved white light with excellent color quality and excellent vision performance. The theoretical and experimental results provide a new perspective for the special effect of $Mn^{2+}$/$Ln^{3+}$ ions on improving the stability and enhancing the luminescence of cesium bromide. Based on this result, it is expected to develop better fluorescent materials.

## Declaration of Competing Interest

The authors declare that they have no known competing financial interests or personal relationships that could have appeared to influence the work reported in this paper.

## Acknowledgments

This work was supported by the National Natural Science Foundation of China (No. 21871079, 11774128), the Natural Science Foundation of Shandong Province (ZR2018JL003, 2019KJJ003), and the National Science Foundation (No. 1945558).

## Appendix A. Supplementary data

Supplementary data to this article can be found online at https://doi.org/10.1016/j.cej.2021.130186.

## References

[1] Q.A. Akkerman, G. Rainò, M.V. Kovalenko, L. Manna, Genesis, challenges and opportunities for colloidal lead halide perovskite nanocrystals, Nat. Mater. 17 (2018) 394–405.
[2] D.J. Gargas, E.M. Chan, A.D. Ostrowski, S. Aloni, M.V.P. Altoe, E.S. Barnard, B. Sanii, J.J. Urban, D.J. Milliron, B.E. Cohen, P.J. Schuck, Engineering bright Sub-10-nm upconverting nanocrystals for single-molecule imaging. Nat. Nanotechnol. 9 (2014) 300-305.
[3] G.J. Hoerder, M. Seibald, D. Baumann, T. Schröder, S. Peschke, P.C. Schmid, T. Tyborski, P. Pust, I. Stoll, M. Bergler, C. Patzig, S. Reißaus, M. Krause, L. Berthold, T. Höche, D. Johrendt, H. Huppertz, Sr $[Li_2Al_2O_2N_2]$: $Eu^{2+}$- A high performance red phosphor to brighten the future, Nat. Commun. 10 (2019) 1824.
[4] Siddha Pimputkar, James S. Speck, Steven P. DenBaars, Shuji Nakamura, Prospects for LED lighting, Nat. Photonics. 3 (4) (2009) 180–182.
[5] P. Pust, P. J. Schmidt, W. Schnick, A revolution in lighting. Nat. Mater. 14(2015) 454-458.
[6] S. Wen, J. Zhou, K. Zheng, A. Bednarkiewicz, X. Liu, D. Jin, Advances in highly doped upconversion nanoparticles, Nat. Commun. 9 (2018) 2415.
[7] W. Zou, C. Visser, J.A. Maduro, M.S. Pshenichnikov, J.C. Hummelen, Broadband dye-sensitized upconversion of near-infrared light, Nat. Photonics. 6 (2012) 560–564.
[8] J. Zhao, D. Jin, E.P. Schartner, Y. Lu, Y. Liu, A.V. Zvyagin, L. Zhang, J.M. Dawes, P. Xi, J.A. Piper, E.M. Goldys, T.M. Monro, Single-nanocrystal sensitivity achieved by enhanced upconversion luminescence, Nat. Nanotechnol. 8 (2013) 729–734.
[9] X.Y. Huang, S.Y. Han, W. Huang, X.G. Liu, Enhancing solar cell efffiffifficiency: the search for luminescent materials as spectral converters, Chem. Soc. Rev. 42 (2013) 173–201.
[10] S. Liu, Y. Liang, Y. Zhu, H. Li, Y. Cai, D. Tu, Full visible spectra emission introduced by crystal-site engineering in β-$Ca_3(PO_4)_2$-type solid solution phosphors for high quality white light emitting diodes application, Chem. Eng. J. 375 (2019), 121976.
[11] X. Huang, Red phosphor converts white LEDs, Nat. Photon. 8 (2014) 748–749.
[12] X.F. Wang, Z.X. Qiu, Y.M. Li, Q.H. Mi, W.L. Zhou, S.Y. Ai, J. Xu, Y.F. Liu, S.X. Lian, Core-shell structured CaS: $Eu^{2+}$@CaZnOS via inward erosion growth to realize a super stable chalcogenide red phosphor, J. Mater. Chem. C 7 (2019) 5931–5936.
[13] L. Wang, R.J. Xie, T. Suehiro, T. Takeda, N. Hirosaki, Down-conversion nitride materials for solid state lighting: recent advances and perspectives, Chem. Rev. 118 (2018) 1951–2009.
[14] M. Pan, W.M. Liao, S.Y. Yin, S.S. Sun, C.Y. Su, Single-phase white-light-emitting and photoluminescent color-tuning coordination assemblies, Chem. Rev. 118 (2018) 8889–8935.
[15] Z. Xia, Y. Zhang, M.S. Molokeev, V.V. Atuchin, Y. Luo, Linear structural evolution induced tunable photoluminescence in clinopyroxene solid-solution phosphors, Sci. Rep. 3 (2013) 3310.
[16] H. Ji, Z. Huang, Z. Xia, M.S. Molokeev, V.V. Atuchin, M. Fang, S. Huang, New yellow-emitting whitlockite-type structure $Sr_{1.75}Ca_{1.25}(PO_4)_2$: $Eu^{2+}$ phosphor for near-UV pumped white light-emitting devices, Inorg. Chem. 53 (2014) 5129–5135.
[17] J.L. Leaño, S.Y. Lin, A. Lazarowska, S. Mahlik, M. Grinberg, C. Liang, W. Zhou, M. S. Molokeev, V.V. Atuchin, Y.T. Tsai, C.C. Lin, H.S. Sheu, R.S. Liu, Green light excitable Ce-doped nitridomagnesoaluminate Sr$[Mg_2Al_2N_4]$ phosphor for white light-emitting diodes, Chem. Mater. 28 (2016) 6822–6825.
[18] L. Sun, B. Devakumar, J. Liang, S. Wang, Q. Sun, X. Huang, Highly efficient $Ce^{3+}$→$Tb^{3+}$ energy transfer induced bright narrowband green emissions from garnet-type $Ca_2YZr_2(AlO_4)_3$:$Ce^{3+}$, $Tb^{3+}$ phosphors for white LEDs with high color rendering index, J. Mater. Chem. 7 (2019) 10471–10480.
[19] L. Sun, B. Devakumar, J. Liang, S. Wang, Q. Sun, X. Huang, A broadband cyanemitting $Ca_2LuZr_2(AlO_4)_3$: $Ce^{3+}$ garnet phosphor for near-ultraviolet-pumped warm-white light-emitting diodes with an improved color rendering index, J. Mater. Chem. C 8 (2020) 1095–1103.
[20] G.C. Adhikari, P.A. Vargas, H.Y. Zhu, P. Zhu, Saponififfication precipitation method for CsPbBr 3 nanocrystals with blue-green tunable emission, J. Phys. Chem. C 123 (2019) 1406–1412.
[21] S. Thapa, G.C. Adhikari, H. Zhu, P. Zhu, Blue-red color-tunable all-inorganic bromide-iodide mixed-halide perovskite nanocrystals using the saponification technique for white-light-emitting diodes, J. Opt. Soc. Am. B 36 (2019) 1616–1622.
[22] L.N. Xu, Y.N. Li, Q.J. Pan, D.S. Wang, S. Li, G.F. Wang, Y.J. Chen, P.F. Zhu, W. P. Qin, Dual-mode light-emitting lanthanide metal−organic frameworks with high water and thermal stability and their application in white LEDs, ACS Appl. Mater. Interfaces 12 (2020) 18934–18943.
[23] H.Y. Xu, W. Yu, K. Pan, G.F. Wang, P.F. Zhu, Confinement and antenna effect for ultrasmall $_Y2_O3$:$E^{u3}$+ nanocrystals supported by MOF with enhanced near-UV Light absorption thereby enhanced luminescence and excellently multifunctional applications, Nano Res. 14 (2021) 720–729.
[24] B. Liu, S. Hu, L. Zhang, P. Xiao, L. Huang, C. Liu, Blue molecular emitter-free and doping-free white organic light-emitting diodes with high color rendering, IEEE Electron Device Lett. 42 (3) (2021) 387–390.
[25] B. Liu, M. Sharma, J. Yu, S. Shendre, C. Hettiarachchi, A. Sharma, A. Yeltik, L. Wang, H. Sun, C. Dang, H. V. Demir, Light-emitting diodes with Cu-doped colloidal quantum wells: from ultrapure green, Tunable Dual-Emission to White Light. Small. 15 (2019), e1901983.
[26] L. Protesescu, S. Yakunin, M.I. Bodnarchuk, F. Krieg, R. Caputo, C.H. Hendon, R. X. Yang, A. Walsh, M.V. Kovalenko, Nanocrystals of cesium lead halide perovskites ($CsPbX_3$, X = Cl, Br, and I): novel optoelectronic materials showing bright emission with wide color gamut, Nano Lett. 15 (2015) 3692–3696.

[27] M. Kim, J.H. Kim, M. Kim, C.S. Kim, J.W. Choi, K. Choi, J.H. Lee, J. Park, Y. C. Kang, S.H. Jin, M. Song, Enhanced photoluminescence quantum efficiency and stability of water assisted CsPbBr 3 perovskite nanocrystals, J. Indust. Eng. Chem. 88 (2020) 84–89.
[28] S. Zou, Y. Liu, J. Li, C. Liu, R. Feng, F. Jiang, Y. Li, J. Song, H. Zeng, M. Hong, X. Chen, Stabilizing cesium lead halide perovskite lattice through Mn(II) substitution for air-stable light-emitting diodes, J. Am. Chem. Soc. 139 (2017) 11443–11450.
[29] Y.F. Mu, W. Zhang, X.X. Guo, G.X. Dong, M. Zhang, T.B. Lu, Water-tolerant lead halide perovskite nanocrystals as efficient photocatalysts for visible-light-driven $CO_2$ reduction in pure water, ChemSusChem. 12 (2019) 4769–4774.
[30] Weijiang Guan, Wenjuan Zhou, Jun Lu, Chao Lu, Luminescent films for chemo and biosensing, Chem. Soc. Rev. 44 (19) (2015) 6981–7009.
[31] Zhiguo Xia, Kenneth R. Poeppelmeier, Chemistry-inspired adaptable framework structures, Acc. Chem. Res. 50 (5) (2017) 1222–1230.
[32] F. Wang, Y. Han, C.S. Lim, Y. Lu, J. Wang, J. Xu, H. Chen, C. Zhang, M. Hong, X. Liu, Simultaneous phase and size control of upconversion nanocrystals through lanthanide doping, Nature 463 (7284) (2010) 1061–1065.
[33] X. Xu, W. Zhang, D. Yang, W. Lu, J. Qiu, S.F. Yu, Phonon-assisted population inversion in lanthanide-doped upconversion $ba_2laf_7$ nanocrystals in glass ceramics, Adv. Mater. 28 (36) (2016) 8045–8050.
[34] Y. Liu, M. Pan, Q. Yang, L. Fu, K. Li, S. Wei, C. Su, Dual-emission from a single phase Eu–Ag metal-organic framework: an alternative way to get white-light phosphor, Chem. Mater. 24 (2012) 1954–1960.
[35] M. Yu, H. Xu, Y. Li, Q. Dai, G. Wang, W. Qin, Morphology luminescence and photovoltaic performance of lanthanide doped $CaWO_4$ nanocrystals, J. Colloid Interf. Sci. 559 (2020) 162–168.
[36] Xun Wang, Qing Peng, Yadong Li, Interface-Mediated Growth of Monodispersed Nanostructures, Acc. Chem. Res. 40 (8) (2007) 635–643.
[37] G. Pan, H. Song, X. Bai, Z. Liu, H. Yu, W. Di, S. Li, L. Fan, X. Ren, S. Lu, Novel energy-transfer route and enhanced luminescent properties in $YVO_4$:$Eu^{3+}$/ $YBO_3$:$Eu^{3+}$ composite, Chem. Mater. 18 (2006) 4526–4532.
[38] B. Cao, Y. Bao, Y. Liu, J. Shang, Z. Zhang, Y. He, Z. Feng, B. Dong, Wide-range and highly-sensitive optical thermometers based on the temperature-dependent energy transfer from Er to Nd in Er/Yb/Nd codoped $NaYF_4$ upconversion nanocrystals, Chem. Eng. J. 385 (2020), 123906.
[39] Y.-Q. Sun, J. Zhang, Y.-M. Chen, G.-Y. Yang, Porous lanthanide-organic open frameworks with helical tubes constructed from interweaving triple-helical and double helical chains, Angew. Chem. Int. Ed. 44 (36) (2005) 5814–5817.
[40] L. Liang, D.B.L. Teh, N.D. Dinh, W. Chen, Q. Chen, Y. Wu, S. Chowdhury, A. Yamanaka, T.C. Sum, C.H. Chen, N.V. Thakor, A.H. All, X. Liu, Upconversion amplifification through dielectric superlensing modulation, Nat. Commun. 10 (2019) 1391.
[41] W.J. Mir, T. Sheikh, H. Arfin, Z. Xia, A. Nag, Lanthanide doping in metal halide perovskite nanocrystals: spectral shifting, quantum cutting and optoelectronic applications, NPG Asia Mater. 12 (1) (2020), https://doi.org/10.1038/s41427-019-0192-0.
[42] C.H. Lu, G.V. Biesold-McGee, Y. Liu, Z. Kang, Z. Lin, Doping and ion substitution in colloidal metal halide perovskite nanocrystals, Chem. Soc. Rev. 49 (2020) 4953–5007.
[43] E. Tenuta, C. Zheng, O. Rubel, Thermodynamic origin of instability in hybrid halide perovskites, Sci. Rep. 6 (2016) 37654.
[44] J.F. Herbst, L.G. Hector, Energetics of the Li amide/Li imide hydrogen storage reaction, Physical Review B. 72 (2005), 125120.
[45] P. Zhu, H. Zhu, G.C. Adhikari, S. Thapa, Spectral optimization of white light from hybrid metal halide perovskites, OSA. Continuum. 6 (2019) 1880–1888.
[46] P. Zhu, H. Zhu, G.C. Adhikari, S. Thapa, Design of circadian white light-emitting diodes with tunable color temperature and nearly perfect color rendition, OSA. Continuum. 8 (2019) 2413–2427.